ATLAS CONF Note

ATLAS-CONF-2023-004

2nd April 2023

Improved W boson Mass Measurement using $\sqrt{s} = 7$ TeV Proton-Proton Collisions with the ATLAS Detector

The ATLAS Collaboration

The W boson mass is one of the most interesting fundamental parameters of the Standard Model of particle physics, as it allows for model-independent probes for effects of new physics. In this work, proton-proton data recorded by the ATLAS detector in 2011, at a center of mass energy of 7 TeV, that were used for the first W boson mass measurement at the LHC, have been reanalyzed with an advanced fitting technique based on a profile likelihood approach. This allows for a reduction of several systematic uncertainties. Advances in the modelling of the parton density functions of the proton in recent years have been taken into account and a more modern PDF set has been chosen as baseline. The updated measurement yields a preliminary value of $m_W = 80360 \pm 5(\text{stat.}) \pm 15(\text{syst.}) = 80360 \pm 16$ MeV, where the first uncertainty component is statistical and the second corresponds to the experimental and physics-modelling systematic uncertainty. This result is compatible with the published value and its uncertainty improved by 15%.

ATLAS-CONF-2023-004
11/05/2023

© 2023 CERN for the benefit of the ATLAS Collaboration.
Reproduction of this article or parts of it is allowed as specified in the CC-BY-4.0 license.

1 Introduction

At lowest order in the electroweak theory, the W boson mass, m_W, can be expressed solely as a function of the Z boson mass, m_Z, the fine-structure constant, α, and the Fermi constant, G_μ. Higher-order corrections introduce an additional dependence of the W boson mass on the gauge couplings and the masses of the heavy particles of the SM, such as the top quark mass, m_t, and the Higgs boson mass, m_H [1, 2].

In extended theories, those loop-corrections receive contributions from additional particles and interactions. The effects of new physics can therefore be probed by comparing the measured and predicted values of m_W in the context of global fits to all relevant SM parameters [3–5]. These fits can also be used to predict the SM value, e.g. $m_W^{\text{pred.}} = 80354 \pm 7$ MeV [4]. The current world average of the experimentally determined W boson mass yields a value of $m_W = 80377 \pm 12$ MeV [6], and is based on measurements at LEP-2 [7], Tevatron [8, 9] and the LHC [10, 11]. The world average does not yet include the latest measurement of m_W from the CDF collaboration [12], which yields a value of $m_W = 80433.5 \pm 9.4$ MeV.

In this paper, we present an updated measurement of the W boson mass, which is based on data from proton–proton collisions at a center-of-mass energy of $\sqrt{s} = 7$ TeV recorded by the ATLAS detector in 2011, i.e. the same dataset as was used for the first measurement of m_W at the LHC [10]. While the understanding of the detector as well as the effects of contributions from electroweak and top quark background processes have not changed, significant progress has been made in the statistical framework on the extraction of m_W from the data: an improved fitting technique based on a profile likelihood (PLH) test statistics [13] has been deployed for the first time in the context of a W boson mass measurement. This technique allows a simultaneous determination of m_W together with a set of nuisance parameters describing the experimental and model uncertainties. The PLH fit also required an update of the multijet background estimate. The profiling of nuisance parameters yields a reduction of systematic uncertainties compared to the template fitting technique used previously, which was based on a χ^2 minimization considering statistical uncertainties only, and where systematic uncertainties were added a posteriori.

In recent years, also the understanding of the parton density functions (PDFs) has been significantly improved, yielding several new sets which have been studied within this work. As a consequence the baseline PDF set was changed from the CT10 [14] to the CT18 set [15], where the latter predicts more conservative associated uncertainties.

This note is structured as follows. After a description of the ATLAS detector in Section 2, the analysis strategy including a summary of the previous work on the detector calibration and background estimation is given in Section 3, while the experimental and model uncertainties are summarized in Section 4. The reanalysis of the W boson mass is described in Section 5. The results are summarized in Section 6.

2 ATLAS detector

The ATLAS experiment [16] is a multipurpose particle detector with a forward-backward symmetric cylindrical geometry. It consists of an inner tracking detector surrounded by a thin superconducting solenoid, electromagnetic and hadronic calorimeters, and a muon spectrometer incorporating three large superconducting toroid magnets.

ATLAS uses a right-handed coordinate system with its origin at the nominal interaction point (IP) in the centre of the detector and the z-axis along the beam pipe. The x-axis points from the IP to the centre of the

LHC ring, and the y-axis points upward. Cylindrical coordinates (r, ϕ) are used in the transverse plane, ϕ being the azimuth around the z-axis. The pseudorapidity is defined in terms of the polar angle θ as $\eta = -\ln\tan(\theta/2)$.

The inner-detector system (ID) is immersed in a 2 T axial magnetic field and provides charged-particle tracking in the range $|\eta| < 2.5$. At small radii, a high-granularity silicon pixel detector covers the vertex region and typically provides three measurements per track. It is followed by the silicon microstrip tracker, which usually provides eight measurement points per track. These silicon detectors are complemented by a gas-filled straw-tube transition radiation tracker, which enables radially extended track reconstruction within $|\eta| = 2.0$. The transition radiation tracker also provides electron identification information based on the fraction of hits (typically 35 in total) above a higher energy-deposit threshold corresponding to transition radiation.

The calorimeter system covers the pseudorapidity range $|\eta| < 4.9$. Within the region $|\eta| < 3.2$, electromagnetic (EM) calorimetry is provided by high-granularity lead/liquid-argon (LAr) calorimeters, with an additional thin LAr presampler covering $|\eta| < 1.8$ to correct for upstream energy-loss fluctuations. The EM calorimeter is divided into a barrel section covering $|\eta| < 1.475$ and two endcap sections covering $1.375 < |\eta| < 3.2$. For $|\eta| < 2.5$ it is divided into three layers in depth, which are finely segmented in η and ϕ. Hadronic calorimetry is provided by a steel/scintillator-tile calorimeter, segmented into three barrel structures within $|\eta| < 1.7$ and two copper/LAr hadronic endcap calorimeters covering $1.5 < |\eta| < 3.2$. The solid-angle coverage is completed with forward copper/LAr and tungsten/LAr calorimeter modules in $3.1 < |\eta| < 4.9$, optimised for electromagnetic and hadronic measurements, respectively.

The muon spectrometer (MS) comprises separate trigger and high-precision tracking chambers measuring the deflection of muons in a magnetic field generated by superconducting air-core toroids. The precision chamber system covers the region $|\eta| < 2.7$ with three layers of monitored drift tubes, complemented by cathode strip chambers in the forward region. The muon trigger system covers the range $|\eta| < 2.4$ with resistive plate chambers in the barrel, and thin gap chambers in the endcap regions.

A three-level trigger system is used to select events for offline analysis [17]. The level-1 trigger is implemented in hardware and uses a subset of detector information to reduce the event rate to a design value of at most 75 kHz. This is followed by two software-based trigger levels which together reduce the event rate to about 300 Hz.

3 Measurement overview and analysis strategy

The kinematic properties of a charged lepton from a W boson decay are characterized by its measured transverse momentum, p_{T}^{ℓ}, pseudorapidity, η_{ℓ}, and azimuthal angle, ϕ_{ℓ}. The mass of the lepton, m_{ℓ}, completes the four-vector. The recoil of initial-state partons against the W boson is described in the transverse plane by the hadronic recoil vector, $\vec{u}_{\mathrm{T}}$. It is reconstructed from the vector sum of the transverse energy of all clusters reconstructed in the calorimeters, excluding energy deposits associated with the decay lepton, and defined as $\vec{u}_{\mathrm{T}} = \sum_i \vec{E}_{\mathrm{T},i}$, where $\vec{E}_{\mathrm{T},i}$ is the vector of the transverse energy of cluster i. The transverse-momentum vector of the decay neutrino, $\vec{p}_{\mathrm{T}}^{\,\nu}$, is inferred from the vector of the missing transverse momentum, $\vec{p}_{\mathrm{T}}^{\,\mathrm{miss}}$, which corresponds to the momentum imbalance in the transverse plane, and is defined as $\vec{p}_{\mathrm{T}}^{\,\mathrm{miss}} = -\left(\vec{p}_{\mathrm{T}}^{\,\ell} + \vec{u}_{\mathrm{T}}\right)$. The W boson transverse mass, m_{T}, is derived from $p_{\mathrm{T}}^{\mathrm{miss}}$ and from the transverse momentum of the charged lepton as $m_{\mathrm{T}} = \sqrt{2p_{\mathrm{T}}^{\ell}p_{\mathrm{T}}^{\mathrm{miss}}(1-\cos\Delta\phi)}$, where $\Delta\phi$ is the azimuthal opening angle between the charged lepton and the missing transverse momentum.

Table 1: Summary of 28 categories and kinematic distributions used in the m_W measurement for the electron and muon decay channels.

Decay channel	$W \to e\nu$	$W \to \mu\nu$
Kinematic distributions	p_{T}^{ℓ}, m_{T}	p_{T}^{ℓ}, m_{T}
Charge categories	W^+, W^-	W^+, W^-
$\lvert\eta_\ell\rvert$ categories	[0, 0.6], [0.6, 1.2], [1.8, 2.4]	[0, 0.8], [0.8, 1.4], [1.4, 2.0], [2.0, 2.4]

The mass of the W boson can be determined from fits to distributions of p_{T}^{ℓ} and m_{T}. The expected final-state distributions, referred to as templates, are simulated for several values of m_W, and include signal and background contributions. The templates are compared to the observed distribution by a profile likelihood approach, as described in more detail in Section 5.1. Predictions for different values of m_W are obtained from a single simulated reference sample, by reweighting the W boson invariant mass according to the analytical Breit–Wigner parameterisation of the W boson resonance.

The final measured value of the W boson mass is obtained from a simultaneous PLH fit in the electron and muon decay channels, and in charge- and $|\eta_\ell|$-dependent categories, as defined in Table 1, following the choices in Ref. [10], separately for p_{T}^{ℓ} and m_{T} distributions. The boundaries of the $|\eta_\ell|$ categories are driven by the amount of passive material in front of the EM calorimeter in the electron channel, and by the structure of the ID and of the MS in the muon channel. The measurements of m_W used in the combination are based on the observed distributions of p_{T}^{ℓ} and m_{T}, which are only partially correlated.

The determination of m_W relies on a very good understanding of the detector response as well as the description of the W boson production and its decay. Significant work has already been done for the detector calibration in the context of Ref. [10] and the same detector corrections including uncertainties are also applied in this analysis. Hence only a brief summary of this aspect is given in Section 3.4. The situation is different for the modelling of the W boson production, where several recent developments have been taken into account, which are discussed in Section 3.5 in more detail. While the previous measurement of m_W was based on a χ^2 compatibility test, a profile likelihood approach was implemented in the current work, allowing to fit and thus constrain experimental as well as modelling systematic uncertainties. The updated fitting method was tested in several steps. In the first step, it was tested that the previous χ^2-based results for m_W are reproduced when using the CT10 PDF set and only statistical uncertainties in the profile likelihood approach. In the second step, the profile likelihood method was applied individually for all measurement categories and the behaviour of the resulting constrained systematic uncertainties has been studied. Finally, a full profile likelihood fit over all categories and decay channels has been performed where the CT18 PDF set has been used as baseline.

3.1 Data samples and event generation

The same data and MC samples as previously used in Ref. [10] build the basis of this analysis: the data sample consists of W boson candidate events, collected in 2011 with the ATLAS detector in proton–proton collisions at the LHC, at a center-of-mass energy of $\sqrt{s} = 7$ TeV. The data taken with all relevant detector systems operational correspond to approximately 4.6 fb^{-1} and 4.1 fb^{-1} of integrated luminosity in the electron and muon channels, respectively.

The POWHEG MC generator [18–20] (v1/r1556) is used for the simulation of the hard-scattering processes of W and Z boson production and decay in the electron, muon, and tau channels, and is interfaced to PYTHIA 8 (v8.170) for the modelling of the parton shower, hadronisation, and underlying event [21, 22], with parameters set according to the AZNLO tune [23]. The CT10 PDF set [14] is used for the hard-scattering processes, whereas the CTEQ6L1 PDF set [24] is used for the parton shower. In the Z boson samples, the effect of virtual photon production (γ^*) and Z/γ^* interference is included. The effect of QED final-state radiation (FSR) is simulated with PHOTOS (v2.154) [25]. Tau lepton decays are handled by PYTHIA 8, taking into account polarisation effects. The W and Z boson event yields are normalised according to their measured cross sections, and uncertainties of 1.8% and 2.3% are assigned to the W^+/Z and W^-/Z production cross-section ratios, respectively [26]. The W production samples assume a value of m_W of 80399 MeV.

Background processes such as the top-quark pair production and the single-top-quark processes are modeled using the MC@NLO MC generator (v4.01) [27–29], interfaced to HERWIG and JIMMY for the parton shower. Gauge-boson pair production (WW, WZ, ZZ) is simulated with HERWIG (v6.520). In all of these samples, the CT10 PDF set is used.

The response of the ATLAS detector is simulated using a program [30] based on GEANT4 4 [31]. The hard-scattering process is overlaid with additional proton–proton interactions, simulated with PYTHIA 8 (v8.165) using the A2 tune [32]. The distribution of the average number of interactions per bunch crossing $\langle\mu\rangle$ spans the range 2.5–16.0, with a mean value of approximately 9.0.

3.2 Object selection

The object definitions stay unchanged compared to Ref. [10]. Electron candidates are reconstructed from clusters of energy deposited in the electromagnetic calorimeter and associated with at least one track in the ID [33, 34]. Quality requirements are applied to the associated tracks in order to reject poorly reconstructed charged-particle trajectories. The energy of the electron is reconstructed from the energy collected in calorimeter cells within an area of size $\Delta\eta \times \Delta\phi = 0.075 \times 0.175$ in the barrel, and 0.125×0.125 in the endcaps. A multivariate regression algorithm, developed and optimised on simulated events, is used to calibrate the energy reconstruction and various corrections are applied. The kinematic properties of the reconstructed electron are inferred from the energy measured in the EM calorimeter, and from the pseudorapidity and azimuth of the associated track. Electron candidates are required to have $p_{\mathrm{T}}^{\ell} > 15$ GeV and $|\eta| < 2.4$ and to fulfil a set of tight identification requirements [33]. As in the legacy result, the pseudorapidity range $1.2 < |\eta| < 1.8$ is excluded from the measurement. Additional isolation requirements on the nearby activity in the ID and calorimeter are applied to improve the background rejection [10].

The muon reconstruction is performed independently in the ID and in the MS, and a combined muon candidate is formed from the combination of a MS track with an ID track, based on the statistical combination of the track parameters [35]. The kinematic properties of the reconstructed muon are defined using the ID track parameters alone, which allows a simpler calibration procedure. Muon candidates are required to have $p_{\mathrm{T}}^{\ell} > 20$ GeV and $|\eta| < 2.4$ [10]. Similarly to the electrons, the rejection of multijet background is increased by applying an isolation requirement [10].

The recoil, $\vec{u}_{\mathrm{T}}$, is reconstructed from the vector sum of the transverse energy of all clusters measured in the calorimeters, as previously defined. The definition of $\vec{u}_{\mathrm{T}}$ and the inferred quantities $p_{\mathrm{T}}^{\mathrm{miss}}$ and m_{T} do not involve the explicit reconstruction of particle jets, to avoid possible threshold effects. Clusters located at a

distance $\Delta R < 0.2$ from the reconstructed electron or muon candidates are not used for the reconstruction of $\vec{u}_{\mathrm{T}}$ [10].

3.3 Signal selection and background estimation

The W boson sample is collected during data-taking with triggers requiring at least one muon candidate with transverse momentum larger than 18 GeV or at least one electron candidate with transverse momentum larger than 20 GeV. The transverse-momentum requirement for the electron candidate was raised to 22 GeV in later data-taking periods to cope with the increased instantaneous luminosity delivered by the LHC. Selected events are required to have a reconstructed primary vertex with at least three associated tracks.

W boson candidate events are selected by requiring exactly one reconstructed electron or muon with $p_{\mathrm{T}}^{\ell} > 30$ GeV. The leptons are required to match the corresponding trigger object. In addition, the reconstructed recoil is required to be $u_{\mathrm{T}} < 30$ GeV, the missing transverse momentum $p_{\mathrm{T}}^{\mathrm{miss}} > 30$ GeV and the transverse mass $m_{\mathrm{T}} > 60$ GeV. A total of $5.89{\times}10^6$ W boson candidate events are selected in the $W \to e\nu$ channel, and $7.84{\times}10^6$ events in the $W \to \mu\nu$ channel, yielding exactly the same events as in Ref. [10].

The resulting selected W boson event sample includes events from various background processes. Background contributions from Z boson, $W \to \tau\nu$, boson pair, and top-quark production are estimated using simulation, while contributions from multijet production are estimated with data-driven techniques. The estimation of the latter is divided into two steps. First, the number of multijet events passing the analysis selection requirements is estimated using a template fit to the $p_{\mathrm{T}}^{\mathrm{miss}}$, m_{T} and the $p_{\mathrm{T}}^{\ell}/m_{\mathrm{T}}$ distributions in background dominated regions. The estimated multijet event yield is expressed as a fraction of the total number of selected events. In the second step, the multijet p_{T}^{ℓ} and m_{T} distributions are extrapolated from anti-isolated control regions to the signal region, keeping the multijet yield fixed. In the previous analysis, the uncertainties in the multijet distributions were propagated to m_W through fluctuations of the extrapolation parameters; an eigenvector decomposition is used in the present analysis.

3.4 Detector calibration

Experimentally, the p_{T}^{ℓ} and $p_{\mathrm{T}}^{\mathrm{miss}}$ distributions are affected by the lepton energy calibration. The latter is also affected by the calibration of the recoil. $Z \to \ell\ell$ event samples are used to calibrate the detector response for leptons and the hadronic recoil. Lepton momentum corrections are derived exploiting the precisely measured value of the Z boson mass, m_Z [36], and the recoil response is calibrated using the expected momentum balance with $p_{\mathrm{T}}^{\ell\ell}$. Identification and reconstruction efficiency corrections are determined from W and Z boson events using the tag-and-probe method [33, 35]. The dependence of these corrections on p_{T}^{ℓ} is important for the measurement of m_W, as it affects the shape of the template distributions.

The calibration methods, published in detail in Ref. [10] yield a precision on the energy and momentum scale for electrons and muons of $O(10^{-4})$, with somewhat larger uncertainty for the muons in high-η region. The response and resolution on the hadronic recoil is determined with a precision of $O(\%)$. The experimental precisions are typically limited by the finite size of the Z boson sample, which is approximately ten times smaller than the W boson sample.

3.5 Physics modelling

Samples of inclusive vector-boson production are produced using the POWHEG MC generator interfaced to PYTHIA 8, henceforth referred to as POWHEG+PYTHIA 8. The W and Z boson samples are reweighted to include the effects of higher-order QCD and electroweak (EW) corrections, as well as the results of fits to measured distributions which improve the agreement of the simulated lepton kinematic distributions with the data. The procedure to account for these corrections is based on the factorisation of the fully differential leptonic Drell–Yan cross section [37] and follows the strategy of the orginal analysis through an event-by-event reweighting, which is also used to estimate systematic uncertainties. In particular, the differential cross section as a function of boson rapidity, $\mathrm{d}\sigma(y)/\mathrm{d}y$, and the angular coefficients, A_i, are modelled with fixed-order perturbative QCD predictions, at $O(\alpha_s^2)$ in the perturbative expansion of the strong coupling constant and using the CT10 PDF set [38]. In addition, several other newer PDF sets, in particular CT14 [39], CT18 [15], MMHT2014 [40] and MSHT20 [41], as well as NNPDF3.1 [42] and NNPDF4.0 [43] have been also studied. The transverse-momentum spectrum at a given rapidity, $\mathrm{d}\sigma(p_\mathrm{T}, y)/(\mathrm{d}p_\mathrm{T}\,\mathrm{d}y) \cdot (\mathrm{d}\sigma(y)/\mathrm{d}y)^{-1}$, is modelled with predictions based on the PYTHIA 8 MC generator.

4 Uncertainties

4.1 Experimental uncertainties

Systematic uncertainties in the determination of m_W are evaluated using pseudodata samples produced from the nominal simulated event samples by varying the parameters corresponding to each source of uncertainty in turn, providing additional signal (and background) templates. For two-sided systematics, two separate sets of templates are produced for the up and down variation, corresponding to a shift at 68% CL. Systematic uncertainties of statistical nature, for example for the electron and muon identification and reconstruction efficiencies, are propagated using a toy MC method by fluctuating nominal efficiency values within their statistical uncertainty, and generating templates for each toy variation. Since toy variations can not be directly included in a profile likelihood fit, a Principal Component Analysis (PCA) [44, 45] is used to transform each toy-based systematic into a set of uncorrelated two-sided uncertainties, preserving the total uncertainty. This approach is used for the statistical uncertainties of electron and muon efficiencies, for the recoil calibration, and for the spin correlation uncertainties.

In total 75 (p_T^ℓ) and 58 (m_T) sources of uncertainties are considered for the electron calibration, including the energy scale and resolution as well as the electron identification, isolation, and trigger efficiencies. Twenty-three of these uncertainties are two-point systematics, while 52 (p_T^ℓ) and 35 (m_T) systematic variations are from the PCA. 83 (p_T^ℓ) and 76 (m_T) sources of uncertainties are taken into account for the muon response, covering the momentum scale and resolution as well as the muon reconstruction, trigger and isolation efficiencies. Here, six two-point systematics and 77 (p_T^ℓ) or 70 (m_T) PCA components are considered. The calibration of the hadronic recoils yields seven (p_T^ℓ) and 36 (m_T) sources of systematic uncertainties. Three of these uncertainties are two-point systematics, while four (p_T^ℓ) and 33 (m_T) PCA variations are taken into account.

Systematic uncertainties related to leptonic and recoil calibrations are statistically dominated. They show large bin-to-bin variations in the kinematic observables which are caused by statistical fluctuations, which can introduce instabilities in the PLH fit. A smoothing procedure is applied to remove the fluctuations in the up and down variations of the corresponding uncertainties, preserving the normalisation of each

variation. The smoothing procedure is applied to the systematic uncertainties of the muon momentum calibration, the electron energy response, and the recoil corrections, but not to the lepton efficiencies and the recoil calibration statistical uncertainties, as those are treated by the PCA. Furthermore, those systematic uncertainties are expected to be symmetric in terms of the source and thus to have a symmetric effect on the variation. Some of the considered envelopes show an artificial asymmetry caused by statistical fluctuations. Hence, the relative uncertainty of the up and the down envelope are symmetrised. The total fit uncertainty was verified not to be significantly affected by the smoothing and symmetrisation procedures.

Propagating all systematic uncertainties as NPs to the PLH complicates the extended likelihood function. Systematic uncertainties which have a negligible impact on the shape or the normalisation can be pruned as they might arise from statistical fluctuations. The shape and the normalisation of a systematic uncertainty are treated independently. The variations and the nominal distribution are normalised to the same area before checking the pruning requirement. The optimal threshold value for the shape is obtained by removing most of the NPs without reducing the total uncertainty by more than 1%. The total number of NPs is determined by counting every systematic uncertainty in every measurement category regardless of whether it is correlated across several measurement categories or not. No pruning on the normalisation is considered. Systematic uncertainties which yield shape differences smaller then 0.01% in each bin for p_{T}^{ℓ} and 0.02% in each bin for m_{T} are pruned, reducing the number of shape systematics by roughly a factor of two. The total change in the uncertainty of the final measurement uncertainty is less than 1% relative, when using the reduced set.

4.2 Electroweak uncertainties

The dominant source of electroweak corrections to W production originates from QED final-state radiation, and is simulated with Photos. The effect of QED initial-state radiation (ISR) is also included through the Pythia8 parton shower. Other sources of electroweak corrections are not included in the simulated event samples, and their full effects are considered as systematic uncertainties. Systematics from missing higher-order electroweak corrections are estimated considering the same sources of uncertainty as in Ref. [10]. They are now however determined at detector level, increasing their impact on m_W by typically 20%.

4.3 QCD modelling uncertainties

Several sources of uncertainty related to the perturbative and non-perturbative modelling of the strong interaction affect the dynamics of the vector-boson production and decay [46–49]. Their impact on the measurement of m_W is assessed through variations of the model parameters of the predictions for the differential cross sections as functions of the boson rapidity, transverse-momentum spectrum at a given rapidity, and angular coefficients.

PDF uncertainties in the rapidity distributions and angular coefficients are evaluated using DYNNLO [50], and are constrained in the fit through their impact on the p_{T}^{ℓ} and m_{T} distributions. The PDF contribution to the model uncertainty is estimated using the Hessian method [51], where each eigenvector of the PDF fit covariance matrix defines a pair of PDF uncertainty variations and a corresponding nuisance parameter in the PLH fit. PDF uncertainties are calculated for the CT10, CT14, CT18, MMHT2014, MSHT20, NNPDF3.1 and NNPDF4.0 sets. The CT10, CT14, CT18 variations correspond to 90% CL, and are rescaled to match the 68% CL.

The impact of PDFs on the W boson p_{T} distribution is evaluated using Pythia8, by reweighting the PDFs in the differential cross section event by event. Pythia8 simulates the emission of up to one jet, according to the corresponding $O(\alpha_{\mathrm{s}})$ cross sections, and models the influence of initial-state gluons on the distributions, allowing a consistent use of PDF sets beyond LO. The PDF variations in Pythia and DYNNLO are synchronized to capture the correlated effect of PDF variations on the boson p_{T}, y and decay distributions. For this analysis, the modeling of the transverse momentum distribution has been verified by comparing the predicted hadronic recoil distribution to the distribution observed for W boson candidate events, recorded during a special proton-proton run at a center of mass energy of 5 TeV under low pile-up conditions, which yield a significantly better hadronic recoil resolution. The observed spectrum agrees with the predicted distributions, within the experimental uncertainties and a precision of about 1%.

Several additional sources of uncertainty affect the W boson p_{T} spectrum predicted by the Pythia8 parton shower model. The uncertainties in the AZ tune parameters [52] have been propagated to the final-state distributions. The initial-state charm and bottom quark masses affect the p_{T} spectrum, and the corresponding uncertainties have been estimated by varying their respective masses by $\pm 0.5\,\mathrm{GeV}$ and $\pm 0.8\,\mathrm{GeV}$, respectively. Uncertainties in the shower evolution are parameterised through variations of the factorisation scale, μ_{F}, by factors of 0.5 and 2.0 with respect to the central choice $\mu_{\mathrm{F}}^2 = p_{\mathrm{T},0}^2 + p_{\mathrm{T}}^2$, where $p_{\mathrm{T},0}$ is an infrared cut-off, and p_{T} is the evolution variable of the parton shower [53]. The variations are applied independently to the light-quark, charm-quark and bottom-quark-induced processes. These uncertainties are propagated by considering relative variations of the p_{T}^W and p_{T}^Z distributions as discussed in Ref. [10]. Differences in the shower model, e.g. between the Pythia8 and Herwig7 predictions, have been found to be negligible.

The accuracy of the NNLO predictions of the angular coefficients is validated by comparison to the Z boson measurement, and extrapolated to W boson production assuming that NNLO predictions have similar accuracy for the W and Z boson processes. Special focus is given to the A_2 angular coefficient, given that a disagreement between data and MC as a function of the Z boson p_{T} has been observed. This disagreement between data and MC has been translated to the W boson production and is taken as additional uncertainty. The overall uncertainties of the angular coefficients are dominated by the experimental uncertainty of the Z boson measurement which is used to validate the theoretical predictions [54].

The effect of missing higher-order corrections on the NNLO predictions of the rapidity distributions as well as the effect of the LHC beam-energy uncertainty of 0.65% have both been found to be negligible and have not been considered further.

5 Reanalysis of the W boson mass

The analysis is performed in two steps. The first step consists in repeating the analysis using the CT10 PDF set and otherwise unchanged systematic uncertainties, and provides a test of the stability of the measurement under the change of test statistic. In a second step, the measurement is updated to recent PDF sets, and a new baseline is chosen.

5.1 Fitting strategy

The previous measurement of the W boson mass consisted in separate template fits to the p_{T}^{ℓ} and m_{T} distributions observed in the different categories. In the fit, the χ^2 of the comparison between data and

simulation was minimized considering statistical uncertainties only; systematic uncertainties were included by varying the parameters determining the templates within their uncertainties, and repeating the fits. The present analysis consist in a simultaneous optimization of m_W, and of nuisance parameters describing systematic uncertainties, through a global profile likelihood fit in all categories. The likelihood function, which describes the compatibility of data and MC distributions, is given by

$$L\left(\mu, \vec{\theta}|\vec{n}\right) = \prod_j \prod_i \text{Poisson}\left(n_{ji}|\nu_{ji}(\mu, \vec{\theta})\right) \cdot \text{Gauss}\left(\vec{\theta}\right), \tag{1}$$

where $\vec{n}$ represents the observed distributions in data, n_{ji} is the number of events observed in data in bin i of the distribution in a given category j. It is the input to the Poisson distribution with expectation $\nu_{ji}(\mu, \vec{\theta}) = S_{ji}(\mu, \vec{\theta}) + B_{ji}(\mu, \vec{\theta})$, of S_{ji} events from signal and B_{ji} events from background contributions. The parameter of interest, μ, represents variations in m_W with respect to a conventional reference. Uncertainties of the signal and background distributions are encapsulated as nuisance parameters (NPs), denoted as $\vec{\theta}$ in Eq. 1, for which a normal probability distribution is assumed. The expected number of events ν_{ji} is parameterised as

$$\begin{aligned} \nu_{\text{ji}}(\mu, \vec{\theta}) = \Phi \times \left[S_{\text{ji}}^{\text{nom}} + \mu \times \left(S_{\text{ji}}^{\mu} - S_{\text{ji}}^{\text{nom}}\right)\right] + \sum_s \theta_s \times \left(S_{\text{ji}}^{p} - S_{\text{ji}}^{\text{nom}}\right) \\ + B_{\text{ji}}^{\text{nom}} + \sum_b \theta_b \times \left(B_{\text{ji}}^{p'} - B_{\text{ji}}^{\text{nom}}\right), \end{aligned} \tag{2}$$

where Φ is an overall, unconstrainted normalisation factor ensuring that the total signal rate always adjusts to the number of events in data, $S_{\text{ji}}^{\text{nom}}$ and $B_{\text{ji}}^{\text{nom}}$ the nominal distribution of signal and background, respectively.

Changes in μ and $\vec{\theta}$ lead to changes in the expected signal and background distributions, that are interpolated using a polynomial morphing procedure. Signal templates for arbitrary values of m_W are obtained from the same simulation sample, which assumes $m_W = 80399$ MeV, through a reweighting of the W-boson Breit-Wigner distribution. Templates representing systematic variations are determined from two-sided one- and two-sigma variations of the corresponding sources of uncertainty. The interpolation procedure used during the PLH fit between these points has been extensively tested and a perfect closure has been observed.

The W boson mass fit is performed for 28 distinct categories and involves 214 (p_{T}^{ℓ}) and 223 (m_{T}) nuisance parameters in addition to the free W boson mass value. In addition to the lepton-related uncertainties, the background uncertainties are described by 11 NPs, and the PDF- and QCD-modelling uncertainties are modeled by 25 and 3 NPs respectively. The impact of electroweak uncertainties is described by 3 NPs. While fitting m_W, the width of the W boson is set to its SM expectation and treated as additional NP. An additional 1.8% luminosity uncertainty is applied as an overall normalisation envelope to the simulated background samples. When relevant, the NPs are applied simultaneously in the W boson signal and background contributions and are typically correlated across the measurement categories. Some of the lepton calibration uncertainties are taken uncorrelated across pseudorapidity regions if they were determined independently in those regions. The uncertainties related to the multijet background estimate are considered uncorrelated in all measurement categories as they were obtained independently. The fitting range is optimised in order to obtain smallest uncertainty on m_W, and it is found to be $30 < p_{\text{T}} < 50$ GeV and $60 < m_{\text{T}} < 100$ GeV. The optimised fitting range is used for all results presented in this note.

The PLH fit has been performed on data in the individual event categories, and in a combination of those. All categories are statistically independent as long as only the p_{T}^{ℓ} or only the m_{T} distributions are taken into account. The correlation between the final p_{T}^{ℓ} and m_{T}-based results for m_W is determined to be 63±3%, from an ensemble of fit results obtained by fluctuating the data and the most probable values of the nuisance parameters within their respective uncertainties. The p_{T}^{ℓ} and m_{T} results are then combined using the BLUE prescription [55]. The p_{T}^{ℓ} fit has a weight of about 95% and largely dominates the final result.

While uncertainties in the PDFs and in the AZ tune parameters have well defined confidence intervals and can be treated as nuisance parameters, this is more questionable for the other uncertainties in the W-boson p_{T} distribution, i.e. the factorisation scale and quark-mass variations. It was verified that the impact of the latter on the final-state distributions is very similar, in shape, to that of the AZ tune parameters, and that these effects are thus not different from the other sources of uncertainty in this respect, and can be treated accordingly.

5.2 Results with CT10nnlo and consistency tests

The PLH fit result using all categories yields a value of $m_W = 80355.1 \pm 15.6$ MeV with the CT10nnlo PDF set, 14.4 MeV lower compared to the previously published result [10]. Improvements in the analysis, e.g. the improvement of the multi-jet evaluation, increase the measured value by 1.9 MeV; the profiling of systematic uncertainties has an impact of −16.3 MeV.

PLH fits are performed considering statistical uncertainties only, and the central values are compared to the published results in each category. Perfect agreement is observed, validating basic aspects of the technical infrastructure of the PLH fit. A comparison between the published, statistical-only and the PLH fit results is shown in Figure 1 for all categories, and for the full result.

In order to study the expected shifts of the central values in a PLH approach, pseudo-data based on the data are produced, where all sources of systematic uncertainty have been varied within their respective uncertainties. Each pseudo-data set was fitted with the nominal PLH model. The resulting spread of the results for the p_{T}^{ℓ}- and m_{T}-fits is shown in Figure 2 and amounts to 16 MeV and 23 MeV for p_{T}^{ℓ} and m_{T}, respectively, indicating the allowed range of variation of the fit result between the published statistical-only fit and the PLH fit.

For the p_{T}^{ℓ} distribution, the PLH fit reduces the value of m_W by 16 MeV compared to the statistical-only template fit, corresponding to one standard deviation of the allowed variation range according to Figure 2. The fit to the m_{T} distribution varies by -12 MeV when incorporating systematic uncertainties into the PLH fit. In Ref. [10], the combined p_{T}^{ℓ} and m_{T} fit results differed by 6 MeV. In the present fit, the p_{T}^{ℓ} fit result is lower than the m_{T} fit result by 18.2 MeV, while the standard deviation for this difference is 17.6 MeV. The difference is driven by the $p_{\mathrm{T}}(W)$ and specific PDF nuisance parameters, which impact the p_{T}^{ℓ}-fit more than the m_{T}-fit and dominate the improvement in the agreement between the observed and simulated p_{T}^{ℓ} distributions.

The distribution of the nuisance parameter pulls is consistent with a normal distribution (Figure 3), indicating an overall correct estimation of the pre-fit uncertainties. The largest pulls are related to the modeling uncertainty of charm-induced production for the W boson p_{T} description; to one specific eigenvector of the CT10nnlo PDF set; to the muon momentum scale extrapolation uncertainty; and to missing higher-order final state radiation corrections.

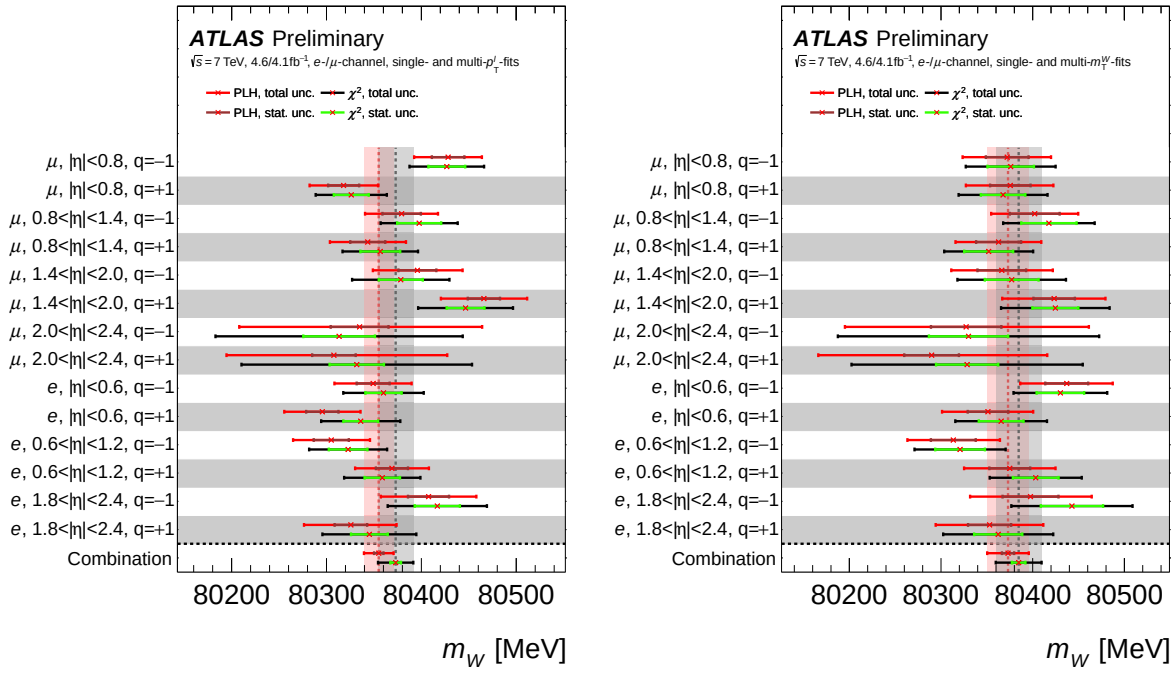

Figure 1: Overview of the m_W fit results in all categories for the p_{T}^{ℓ} (left) and the m_{T} (right) distributions, with the CT10nnlo PDF set. The results are determined using a PLH approach and in comparison with a χ^2-minimization approach using statistical uncertainties only, following the previous measurement [10]. Also shown is the result when using all categories simultaneously.

For the PLH fit using the CT18 PDF set as discussed later in Section 5.3, the list of largest pulls is similar, with two eigenvectors of CT18 PDF set replacing one eigenvector of the CT10nnlo PDF set. The NPs that are most constrained typically correspond to CT18 PDF eigenvector variations. These variations are not normalised prior to the fit, so the fit can constrain them in terms of normalisation to better match what is allowed by the data and other systematic uncertainties.

5.3 PDF dependence and final results

The impact of the profiling on the PDF uncertainties has been studied by performing the fit using the CT14, CT18, MMHT2014, MSHT20, NNPDF3.1 and NNPDF4.0 PDF sets. Since the kinematic distributions as well as the signal yields in the different categories have an additional constraining power on the PDFs, it is expected that the fitted values of m_W get closer together as well as their uncertainties are reduced, when comparing the results to a fit where the PDFs are not profiled. The results of full fits for all considered PDF sets are summarized in Table 2 and Figure 4. While CT10, CT14, MMHT2014 and MSHT20 are within 4 MeV from the CT18 result, a significant deviation is observed for NNPDF3.1 and NNPDF4.0, with central values for m_W which are up to 18 MeV lower compared to the CT18 result. However, as expected the observed spread of m_W values between the different PDF sets is smaller than for unprofiled fits, which amounts to about 28 MeV.

The signal normalisation factors (Φ in Eq. 2) obtained from the combined PLH fits indicate the quality of the description of the W-boson cross sections at $\sqrt{s}$ = 7 TeV by the different PDF sets. For most

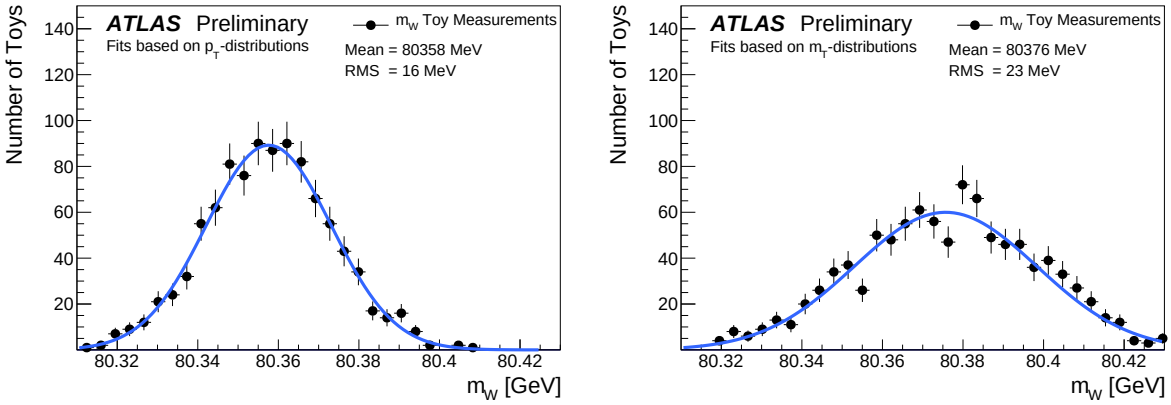

Figure 2: Spread of m_W fit results for 1000 random variations of all sources of systematic uncertainty, using the p_{T}^{ℓ} distribution (left) and the m_{T} distribution (right), and the CT10nnlo PDF set.

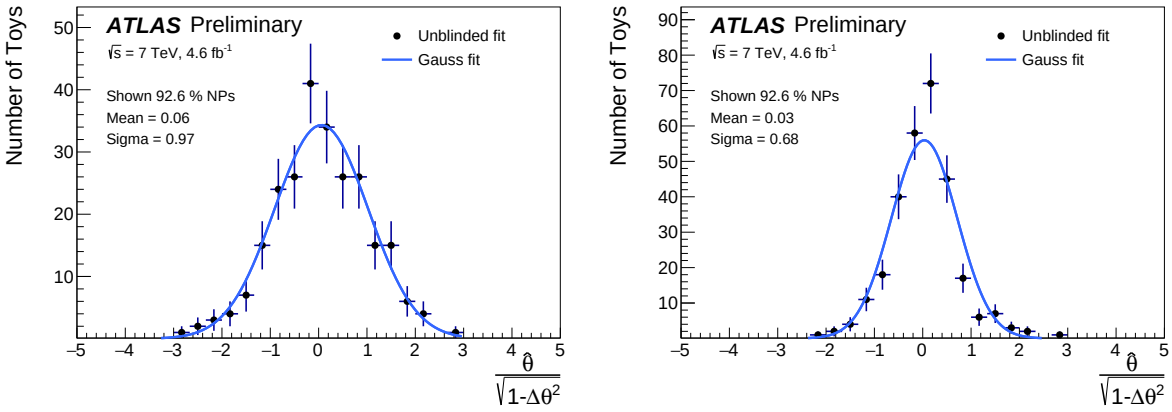

Figure 3: Distribution of pull significances for all individual NPs in the combined PLH fits using the p_{T}^{ℓ} (left) and the m_{T} (right) distributions.

sets, the normalisation factors are compatible with unity within their uncertainties, except for NNPDF4.0, which yields factors of 0.975 ± 0.004 for both the p_{T}^{ℓ} and m_{T} fits. A similiar discrepancy is observed without profiling the PDF uncertainties. Concurrent observations are reported by the LHC-Tevatron m_W combination working group in Ref. [56]. In addition, significant discrepancies between NNPDF4.0 and the data are observed for the measured Z-boson rapidity distribution, in Ref. [56] at $\sqrt{s} = 7$ TeV, and in Ref. [57] at $\sqrt{s} = 8$ TeV. This PDF set is therefore disfavoured by the data and discarded from the present discussion.

The CT18 PDF set, being the most recent of the CTEQ set family, is chosen to define the nominal central value. It also yields the most conservative total uncertainty among all considered PDF sets and is compatible with most other PDF sets that have been studied. For this PDF set, the combination of fit results using the p_{T}^{ℓ} and m_{T} distributions yields a value of $m_W = 80360.4 \pm 16.3$ MeV. A reduction in nearly all systematic uncertainties is seen in the PLH fit compared to the previous results, where the largest improvements of 2-2.5 MeV are observed due to the PDF and QCD-modelling uncertainties profiling.

Figure 5 shows the ten nuisance parameters inducing the largest shift of the m_W central value in the

Table 2: Overview of fitted values of the W boson mass for different PDF sets. The reported uncertainties are the total uncertainties.

PDF-Set	p_{T}^{ℓ} [MeV]	m_{T} [MeV]	combined [MeV]
CT10	$80355.6^{+15.8}_{-15.7}$	$80378.1^{+24.4}_{-24.8}$	$80355.8^{+15.7}_{-15.7}$
CT14	$80358.0^{+16.3}_{-16.3}$	$80388.8^{+25.2}_{-25.5}$	$80358.4^{+16.3}_{-16.3}$
CT18	$80360.1^{+16.3}_{-16.3}$	$80382.2^{+25.3}_{-25.3}$	$80360.4^{+16.3}_{-16.3}$
MMHT2014	$80360.3^{+15.9}_{-15.9}$	$80386.2^{+23.9}_{-24.4}$	$80361.0^{+15.9}_{-15.9}$
MSHT20	$80358.9^{+13.0}_{-16.3}$	$80379.4^{+24.6}_{-25.1}$	$80356.3^{+14.6}_{-14.6}$
NNPDF3.1	$80344.7^{+15.6}_{-15.5}$	$80354.3^{+23.6}_{-23.7}$	$80345.0^{+15.5}_{-15.5}$
NNPDF4.0	$80342.2^{+15.3}_{-15.3}$	$80354.3^{+22.3}_{-22.4}$	$80342.9^{+15.3}_{-15.3}$

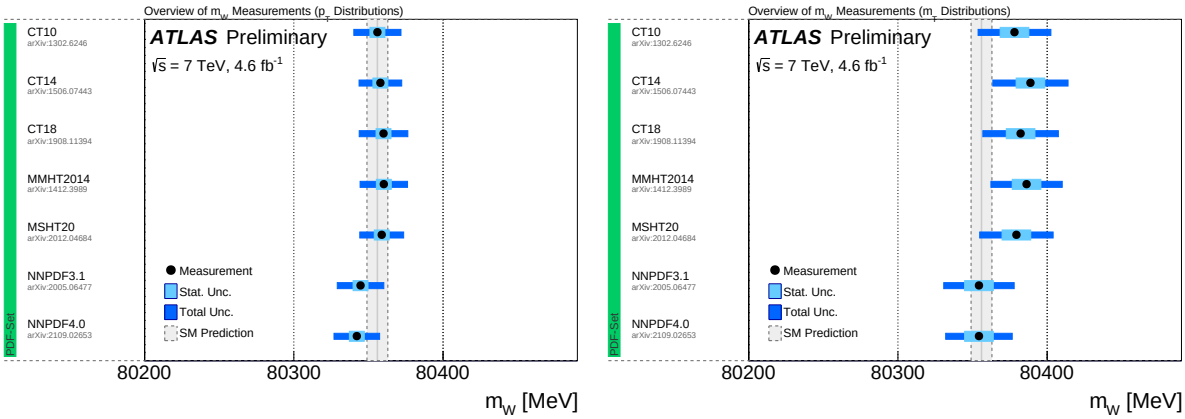

Figure 4: Fitted m_W values for different PDF-Sets using the p_{T}^{ℓ} distribution (left) and m_{T} distribution (right).

combined PLH fits with the CT18 PDF set. The largest impact is due to the first eigenvector of the CT18 PDF. A summary of the impacts of various groups of systematic uncertainties is given in Table 3. A difference of 22 MeV between p_{T}^{ℓ} and m_{T} fits is observed for the CT18 PDF set, which is compatible at 1.3σ level.

Table 3: Impact of the different uncertainty categories on the total uncertainty of the W boson mass measurement using PLH and the CT18 PDF-Set. The impact of each group of systematic uncertainties is defined as the quadratic difference between the total fit uncertainty, and the fit uncertainty obtained excluding this group.

Obs.	Mean [MeV]	Elec. Unc.	PDF Unc.	Muon Unc.	EW Unc.	PS & A_i Unc.	Bkg. Unc.	Γ_W Unc.	MC stat. Unc.	Lumi Unc.	Recoil Unc.	Total sys.	Data stat.	Total Unc.
p_{T}^{ℓ}	80360.1	8.0	7.7	7.0	6.0	4.7	2.4	2.0	1.9	1.2	0.6	15.5	4.9	16.3
m_{T}	80382.2	9.2	14.6	9.8	5.9	10.3	6.0	7.0	2.4	1.8	11.7	24.4	6.7	25.3

An overview of selected pre- and post-fit distributions of p_{T}^{ℓ} and m_{T} is shown in Figure 6, where a general better agreement can be observed for the post-fit case.

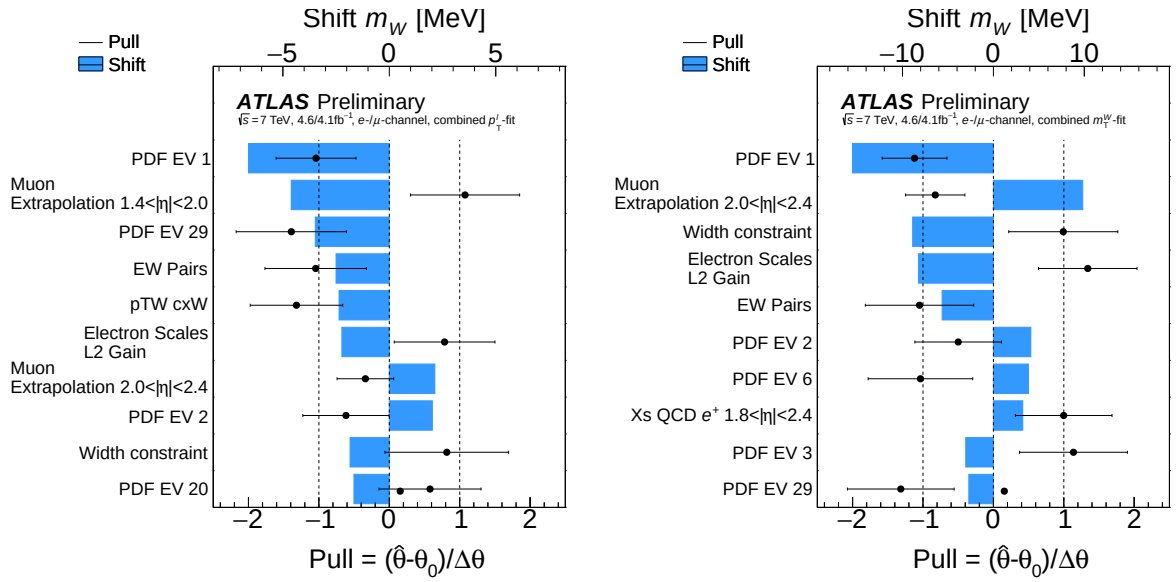

Figure 5: Ranking of 10 nuisance parameters inducing the largest shift of the m_W central value in the combined PLH fits using the p_{T}^{ℓ} (left) and the m_{T} (right) distributions with the CT18 PDF set. The shifts are calculated by multiplying the post-fit pull value of a given NP with its pre-fit impact on the central value (pre-fit impact is calculated with no pull and a constraint of ±1).

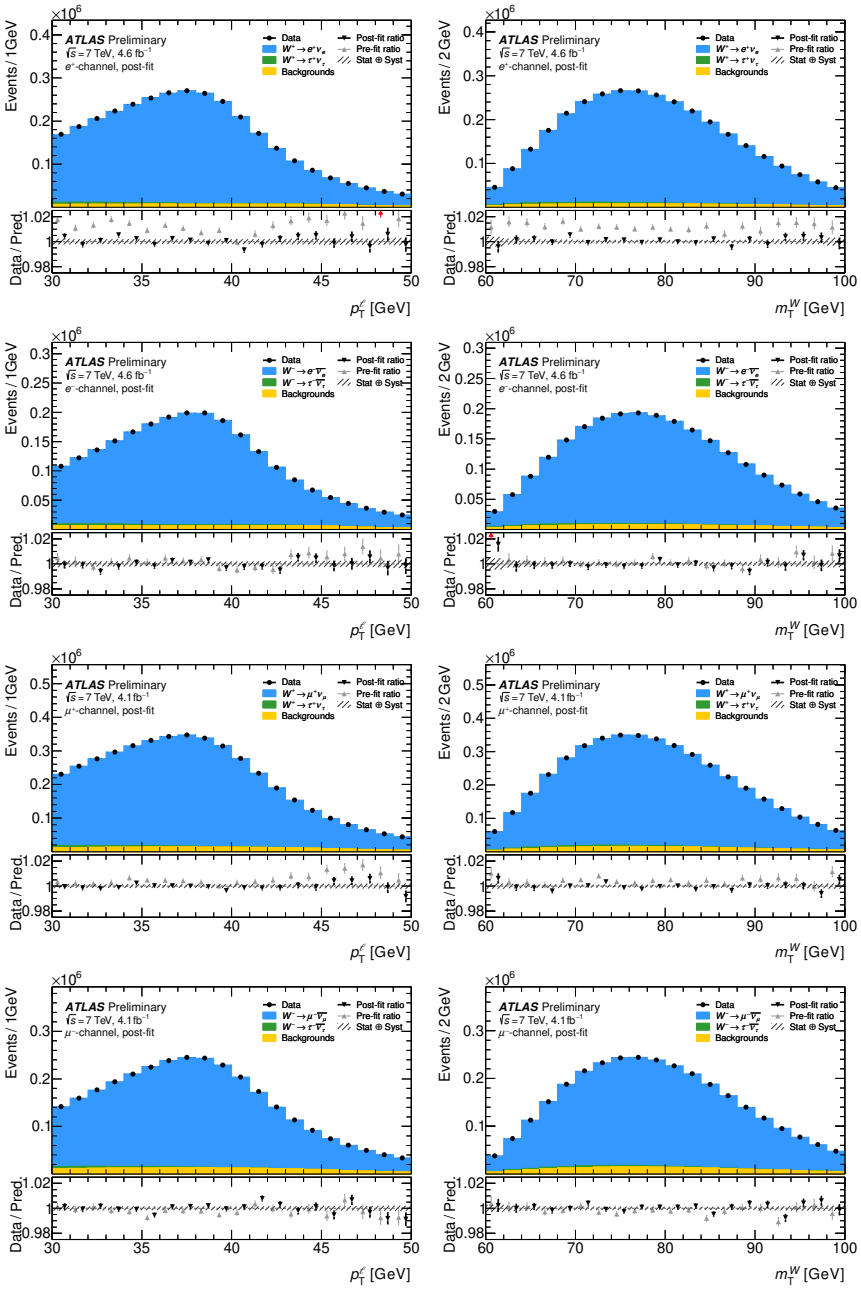

Figure 6: Post-fit distributions of p_{T}^{ℓ} (left) and m_{T} (right) with data and MC for $W^+ \to e^+\nu_e$ (first row), $W^- \to e^-\overline{\nu}_e$ (second row), $W^+ \to \mu^+\nu_\mu$ (third row), $W^- \to \mu^-\overline{\nu}_\mu$ (fourth row), inclusive over all η regions, and using the CT18 PDF set. The ratio indicates also the difference to the data before the fit.

6 Conclusion

This note reports on a reanalysis of the published W boson mass measurement, using an improved fitting technique and updated proton parton density functions. The measurement is based on proton–proton collision data recorded in 2011 at a centre-of-mass energy of $\sqrt{s} = 7$ TeV at the LHC, and corresponding to an integrated luminosity of 4.6 fb^{-1}.

The measurements of m_W using the p_{T}^{ℓ} and m_{T} distributions are found to be consistent and their combination yields a preliminary value of

$$m_W = 80360 \pm 5(\text{stat.}) \pm 15(\text{syst.}) = 80360 \pm 16 \text{ MeV},$$

where the first uncertainty component is statistical and the second corresponds to systematic uncertainties. The compatibility of the measured value with the Standard Model expectation is illustrated in Figure 7, together with selected previous measurements, including the first measurement of the W boson mass at ATLAS which yields a value of $m_W = 80370 \pm 19$ MeV. A decrease of the central value by 10 MeV and a reduction of the total uncertainty by 3 MeV is observed, in agreement with the expectation from toy Monte Carlo studies. The two-dimensional 68% and 95% confidence limits for the predictions of m_W and m_t, in the context of the Standard Model electroweak fit, are shown in Figure 8, and are compared to the present measurement of m_W and to the direct measurement of the top quark mass by ATLAS [58]. No deviation from the SM expectation is observed.

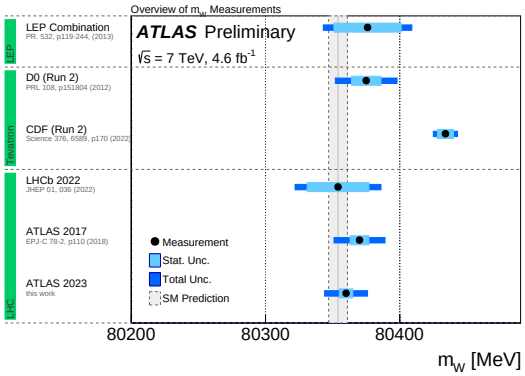

Figure 7: The measured value of m_W is compared to SM prediction from the global electroweak fit [4], and to the combined values of m_W measured at LEP [7], Tevatron [8, 9] and the LHC [10, 11].

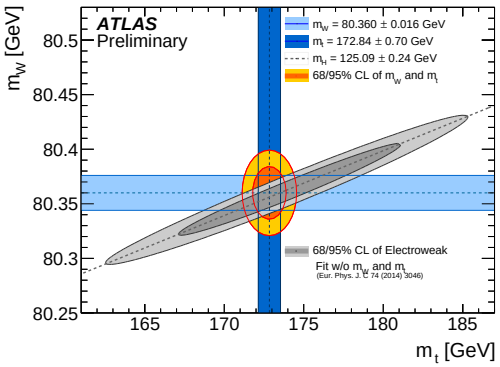

Figure 8: The 68% and 95% confidence-level contours of the m_W and m_t indirect determinations from the global electroweak fit are compared to the 68% and 95% confidence-level contours of the ATLAS measurements of the top quark and W boson masses.

References

[1] A. Sirlin, *Radiative corrections in the $SU(2)_L \times U(1)$ theory: A simple renormalization framework*, Phys. Rev. D **22** (1980) 971 (cit. on p. 2).

[2] M. Awramik, M. Czakon, A. Freitas and G. Weiglein,
Precise prediction for the W-boson mass in the standard model, Phys. Rev. D **69** (2004) 053006, arXiv: hep-ph/0311148 (cit. on p. 2).

[3] J. de Blas, M. Pierini, L. Reina and L. Silvestrini, *Impact of the Recent Measurements of the Top-Quark and W-Boson Masses on Electroweak Precision Fits*,
Phys. Rev. Lett. **129** (2022) 271801, arXiv: 2204.04204 [hep-ph] (cit. on p. 2).

[4] J. Haller, A. Hoecker, R. Kogler, K. Mönig and J. Stelzer,
Status of the global electroweak fit with Gfitter in the light of new precision measurements,
PoS **ICHEP2022** (2022) 897, arXiv: 2211.07665 [hep-ph] (cit. on pp. 2, 17).

[5] J. Erler, 'Global fits to electroweak data using GAPP', *QCD and weak boson physics in Run II. Proceedings, Batavia, IL, March 4-6, June 3-4, November 4-6, 1999*,
arXiv: hep-ph/0005084 [hep-ph] (cit. on p. 2).

[6] R. L. Workman et al., *Review of Particle Physics*, PTEP **2022** (2022) 083C01 (cit. on p. 2).

[7] The ALEPH Collaboration, The DELPHI Collaboration, The L3 Collaboration, The OPAL Collaboration, The LEP Electroweak Working Group,
Electroweak Measurements in Electron-Positron Collisions at W-Boson-Pair Energies at LEP,
Phys. Rept. **532** (2013) 118, arXiv: 1302.3415 [hep-ex] (cit. on pp. 2, 17).

[8] CDF Collaboration, *Precise measurement of the W-boson mass with the CDF II detector*,
Phys. Rev. Lett. **108** (2012) 151803, arXiv: 1203.0275 [hep-ex] (cit. on pp. 2, 17).

[9] D0 Collaboration, *Measurement of the W boson mass with the D0 detector*,
Phys. Rev. D **89** (2014) 012005, arXiv: 1310.8628 [hep-ex] (cit. on pp. 2, 17).

[10] ATLAS Collaboration,
Measurement of the W-boson mass in pp collisions at $\sqrt{s} = 7$ TeV with the ATLAS detector,
Eur. Phys. J. C **78** (2018) 110, arXiv: 1701.07240 [hep-ex] (cit. on pp. 2, 4–6, 8, 9, 11, 12, 17), Erratum: Eur. Phys. J. C **78** (2018) 898.

[11] R. Aaij et al., *Measurement of the W boson mass*, JHEP **01** (2022) 036,
arXiv: 2109.01113 [hep-ex] (cit. on pp. 2, 17).

[12] CDF Collaboration, *High-precision measurement of the W boson mass with the CDF II detector*,
Science **376** (2022) 170 (cit. on p. 2).

[13] G. Cowan, K. Cranmer, E. Gross and O. Vitells,
Asymptotic formulae for likelihood-based tests of new physics, Eur. Phys. J. C **71** (2011) 1554,
arXiv: 1007.1727 [physics.data-an] (cit. on p. 2), Erratum: Eur. Phys. J. C **73** (2013) 2501.

[14] H.-L. Lai et al., *New parton distributions for collider physics*, Phys. Rev. D **82** (2010) 074024,
arXiv: 1007.2241 [hep-ph] (cit. on pp. 2, 5).

[15] T.-J. Hou et al.,
New CTEQ global analysis of quantum chromodynamics with high-precision data from the LHC,
Phys. Rev. D **103** (2021) 014013, arXiv: 1912.10053 [hep-ph] (cit. on pp. 2, 7).

[16] ATLAS Collaboration, *The ATLAS Experiment at the CERN Large Hadron Collider*,
JINST **3** (2008) S08003 (cit. on p. 2).

[17] ATLAS Collaboration, *Performance of the ATLAS Trigger System in 2010*,
Eur. Phys. J. C **72** (2012) 1849, arXiv: 1110.1530 [hep-ex] (cit. on p. 3).

[18] P. Nason, *A new method for combining NLO QCD with shower Monte Carlo algorithms*, JHEP **11** (2004) 040, arXiv: hep-ph/0409146 (cit. on p. 5).

[19] S. Frixione, P. Nason and C. Oleari, *Matching NLO QCD computations with parton shower simulations: the POWHEG method*, JHEP **11** (2007) 070, arXiv: 0709.2092 [hep-ph] (cit. on p. 5).

[20] S. Alioli, P. Nason, C. Oleari and E. Re, *A general framework for implementing NLO calculations in shower Monte Carlo programs: the POWHEG BOX*, JHEP **06** (2010) 043, arXiv: 1002.2581 [hep-ph] (cit. on p. 5).

[21] T. Sjöstrand, S. Mrenna and P. Z. Skands, *PYTHIA 6.4 physics and manual*, JHEP **05** (2006) 026, arXiv: hep-ph/0603175 (cit. on p. 5).

[22] T. Sjöstrand, S. Mrenna and P. Skands, *A brief introduction to PYTHIA 8.1*, Comput. Phys. Commun. **178** (2008) 852, arXiv: 0710.3820 [hep-ph] (cit. on p. 5).

[23] ATLAS Collaboration, *Measurement of the Z/γ^* boson transverse momentum distribution in pp collisions at $\sqrt{s} = 7$ TeV with the ATLAS detector*, JHEP **09** (2014) 145, arXiv: 1406.3660 [hep-ex] (cit. on p. 5).

[24] J. Pumplin et al., *New Generation of Parton Distributions with Uncertainties from Global QCD Analysis*, JHEP **07** (2002) 012, arXiv: hep-ph/0201195 (cit. on p. 5).

[25] P. Golonka and Z. Was, *PHOTOS Monte Carlo: a precision tool for QED corrections in Z and W decays*, Eur. Phys. J. C **45** (2006) 97, arXiv: hep-ph/0506026 (cit. on p. 5).

[26] ATLAS Collaboration, *Precision measurement and interpretation of inclusive W^+, W^- and Z/γ^* production cross sections with the ATLAS detector*, Eur. Phys. J. C **77** (2017) 367, arXiv: 1612.03016 [hep-ex] (cit. on p. 5).

[27] S. Frixione and B. R. Webber, *Matching NLO QCD computations and parton shower simulations*, JHEP **06** (2002) 029, arXiv: hep-ph/0204244 (cit. on p. 5).

[28] S. Frixione, P. Nason and B. R. Webber, *Matching NLO QCD and parton showers in heavy flavour production*, JHEP **08** (2003) 007, arXiv: hep-ph/0305252 (cit. on p. 5).

[29] S. Frixione, E. Laenen, P. Motylinski and B. R. Webber, *Single-top production in MC@NLO*, JHEP **03** (2006) 092, arXiv: hep-ph/0512250 (cit. on p. 5).

[30] ATLAS Collaboration, *The ATLAS Simulation Infrastructure*, Eur. Phys. J. C **70** (2010) 823, arXiv: 1005.4568 [physics.ins-det] (cit. on p. 5).

[31] GEANT4 Collaboration, S. Agostinelli et al., *GEANT4 – a simulation toolkit*, Nucl. Instrum. Meth. A **506** (2003) 250 (cit. on p. 5).

[32] ATLAS Collaboration, *Summary of ATLAS Pythia 8 tunes*, ATL-PHYS-PUB-2012-003, 2012, URL: https://cds.cern.ch/record/1474107 (cit. on p. 5).

[33] ATLAS Collaboration, *Electron reconstruction and identification efficiency measurements with the ATLAS detector using the 2011 LHC proton–proton collision data*, Eur. Phys. J. C **74** (2014) 2941, arXiv: 1404.2240 [hep-ex] (cit. on pp. 5, 6).

[34] ATLAS Collaboration,
Electron and photon energy calibration with the ATLAS detector using LHC Run 1 data,
Eur. Phys. J. C **74** (2014) 3071, arXiv: 1407.5063 [hep-ex] (cit. on p. 5).

[35] ATLAS Collaboration, *Measurement of the muon reconstruction performance of the ATLAS detector using 2011 and 2012 LHC proton–proton collision data*, Eur. Phys. J. C **74** (2014) 3130, arXiv: 1407.3935 [hep-ex] (cit. on pp. 5, 6).

[36] The ALEPH Collaboration, The DELPHI Collaboration, The L3 Collaboration, The OPAL Collaboration, The SLD Collaboration, The LEP Electroweak Working Group, The SLD Electroweak and Heavy Flavour Groups, *Precision electroweak measurements on the Z resonance*, Phys. Rept. **427** (2006) 257, arXiv: hep-ex/0509008 (cit. on p. 6).

[37] S. D. Drell and T.-M. Yan,
Massive Lepton Pair Production in Hadron-Hadron Collisions at High-Energies,
Phys. Rev. Lett. **25** (1970) 316, [Erratum: Phys. Rev. Lett.25,902(1970)] (cit. on p. 7).

[38] J. Gao et al., *CT10 next-to-next-to-leading order global analysis of QCD*,
Phys. Rev. D **89** (2014) 033009, arXiv: 1302.6246 [hep-ph] (cit. on p. 7).

[39] S. Dulat et al.,
New parton distribution functions from a global analysis of quantum chromodynamics,
Phys. Rev. D **93** (2016) 033006, arXiv: 1506.07443 [hep-ph] (cit. on p. 7).

[40] L. A. Harland-Lang, A. D. Martin, P. Motylinski and R. S. Thorne,
Parton distributions in the LHC era: MMHT 2014 PDFs, Eur. Phys. J. C **75** (2015) 204,
arXiv: 1412.3989 [hep-ph] (cit. on p. 7).

[41] S. Bailey, T. Cridge, L. A. Harland-Lang, A. D. Martin and R. S. Thorne,
Parton distributions from LHC, HERA, Tevatron and fixed target data: MSHT20 PDFs,
Eur. Phys. J. C **81** (2021) 341, arXiv: 2012.04684 [hep-ph] (cit. on p. 7).

[42] R. D. Ball et al., *Parton distributions from high-precision collider data*,
Eur. Phys. J. C **77** (2017) 663, arXiv: 1706.00428 [hep-ph] (cit. on p. 7).

[43] R. D. Ball et al., *The Path to Proton Structure at One-Percent Accuracy*, (2021),
arXiv: 2109.02653 [hep-ph] (cit. on p. 7).

[44] K. P. F.R.S., *LIII. On lines and planes of closest fit to systems of points in space*,
The London, Edinburgh, and Dublin Philosophical Magazine and Journal of Science **2** (1901) 559,
URL: https://doi.org/10.1080/14786440109462720 (cit. on p. 7).

[45] H. Hotelling, *Analysis of a complex of statistical variables into principal components*,
Journal of Educational Psychology (1933) 417, URL: https://doi.org/10.1037/h0071325
(cit. on p. 7).

[46] M. Krasny, F. Dydak, F. Fayette, W. Placzek and A. Siodmok,
$\Delta M_W \leq 10 MeV/c^2$ *at the LHC: a forlorn hope?*, Eur. Phys. J. C **69** (2010) 379,
arXiv: 1004.2597 [hep-ex] (cit. on p. 8).

[47] M. Krasny, F. Fayette, W. Placzek and A. Siodmok,
Z-boson as 'the standard candle' for high precision W-boson physics at LHC,
Eur. Phys. J. C **51** (2007) 607, arXiv: hep-ph/0702251 (cit. on p. 8).

[48] F. Fayette, M. Krasny, W. Placzek and A. Siodmok, *Measurement of* $M_{W^+} - M_{W^-}$ *at LHC*,
Eur. Phys. J. C **63** (2009) 33, arXiv: 0812.2571 [hep-ph] (cit. on p. 8).

[49] G. Bozzi, L. Citelli and A. Vicini, *Parton density function uncertainties on the W boson mass measurement from the lepton transverse momentum distribution*, Phys. Rev. D **91** (2015) 113005, arXiv: 1501.05587 [hep-ph] (cit. on p. 8).

[50] S. Catani, L. Cieri, G. Ferrera, D. de Florian and M. Grazzini, *Vector boson production at hadron colliders: a fully exclusive QCD calculation at NNLO*, Phys. Rev. Lett. **103** (2009) 082001, arXiv: 0903.2120 [hep-ph] (cit. on p. 8).

[51] J. Pumplin et al., *Uncertainties of predictions from parton distribution functions. II. The Hessian method*, Phys. Rev. D **65** (2001) 014013, arXiv: hep-ph/0101032 (cit. on p. 8).

[52] ATLAS Collaboration, *Measurement of the Z/γ^* boson transverse momentum distribution in pp collisions at $\sqrt{s} = 7$ TeV with the ATLAS detector*, JHEP **09** (2014) 145, arXiv: 1406.3660 [hep-ex] (cit. on p. 9).

[53] T. Sjöstrand and P. Z. Skands, *Transverse-momentum-ordered showers and interleaved multiple interactions*, Eur. Phys. J. C **39** (2005) 129, arXiv: hep-ph/0408302 (cit. on p. 9).

[54] ATLAS Collaboration, *Measurement of angular correlations in Drell-Yan lepton pairs to probe Z/γ^* boson transverse momentum at $\sqrt{s} = 7$ TeV with the ATLAS detector*, Phys. Lett. B **720** (2013) 32, arXiv: 1211.6899 [hep-ex] (cit. on p. 9).

[55] L. Lyons, D. Gibaut and P. Clifford, *How to Combine Correlated Estimates of a Single Physical Quantity*, Nucl. Instrum. Meth. A **270** (1988) 110 (cit. on p. 11).

[56] LHC–TeVatron W-boson mass combination working group, *Towards a combination of LHC and TeVatron W-boson mass measurements*, CERN-LPCC-2022-06, FERMILAB-TM-2779-V, 2022, URL: https://cds.cern.ch/record/2815187 (cit. on p. 13).

[57] ATLAS Collaboration, *A precise measurement of the Z-boson double-differential transverse momentum and rapidity distributions in the full phase space of the decay leptons with the ATLAS experiment at $\sqrt{s} = 8$ TeV*, ATLAS-CONF-2023-013, 2023 (cit. on p. 13).

[58] ATLAS Collaboration, *Measurement of the top quark mass in the $t\bar{t} \to$ lepton+jets channel from $\sqrt{s} = 8$ TeV ATLAS data and combination with previous results*, Eur. Phys. J. C **79** (2019) 290, arXiv: 1810.01772 [hep-ex] (cit. on p. 17).

Appendix

Figure 9 compares the PLH fit results of the individual measurement categories as well as the combination of all between the PDF set CT10 and CT18.

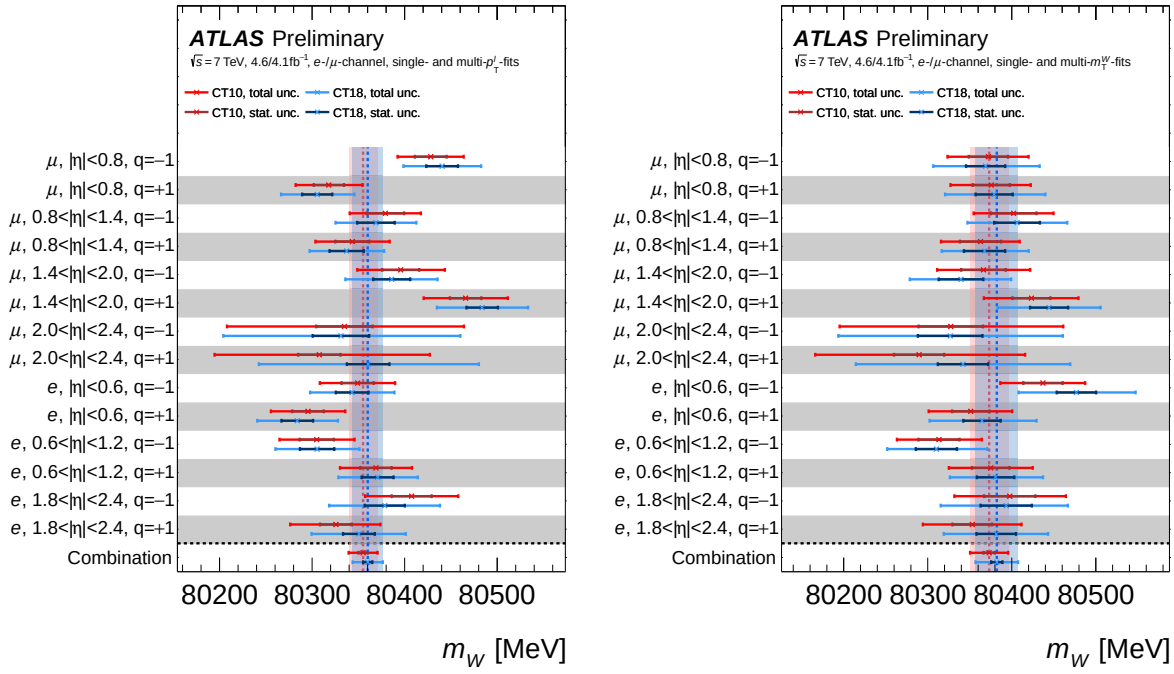

Figure 9: Overview of the m_W fit results in all categories for the p_{T}^{ℓ} (left) and the m_{T} (right) distributions, with the CT10nnlo and CT18 PDF set. Also shown is the result when using all categories simultaneously.

Figure 10 shows the ten nuisance parameters with the largest post-fit impact on m_W in the combined PLH fits with the CT18 PDF set.

Figure 11 shows the post-fit normalization factors for the signal sample for different PDF sets including their postfit uncertainties. The central values of the normalization factors without PDF profiling in the combined PLH fit are also indicated.

Figures 12, 13 and 14 show $W \rightarrow \mu\nu$ candidate events.

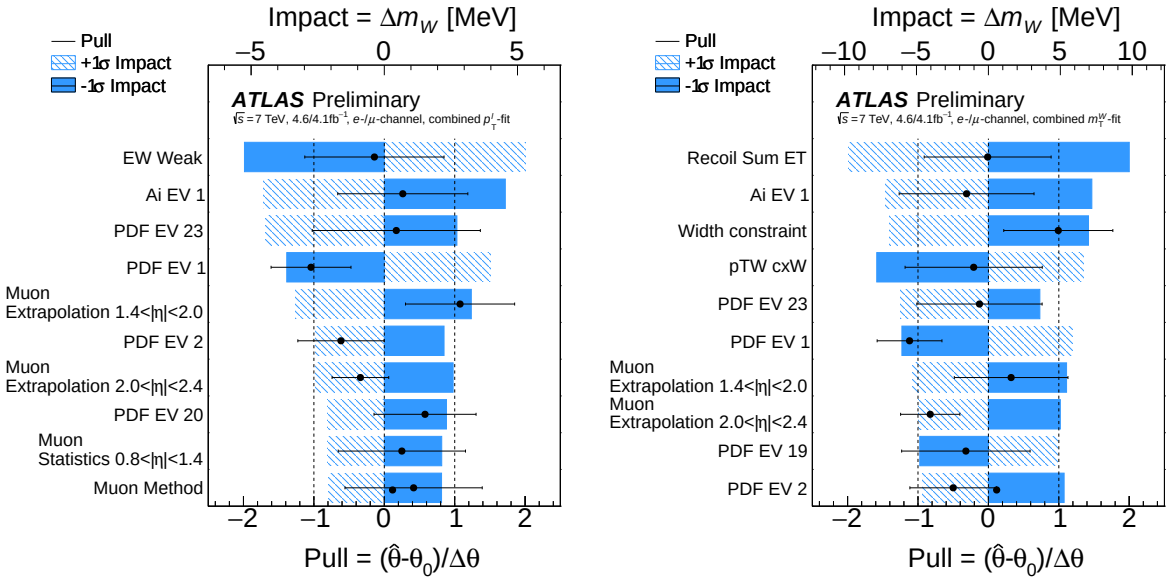

Figure 10: Ranking of 10 nuisance parameters with the largest post-fit impact on m_W in the combined PLH fits using the p_{T}^{ℓ} (left) and the m_{T} (right) distributions with the CT18 PDF set.

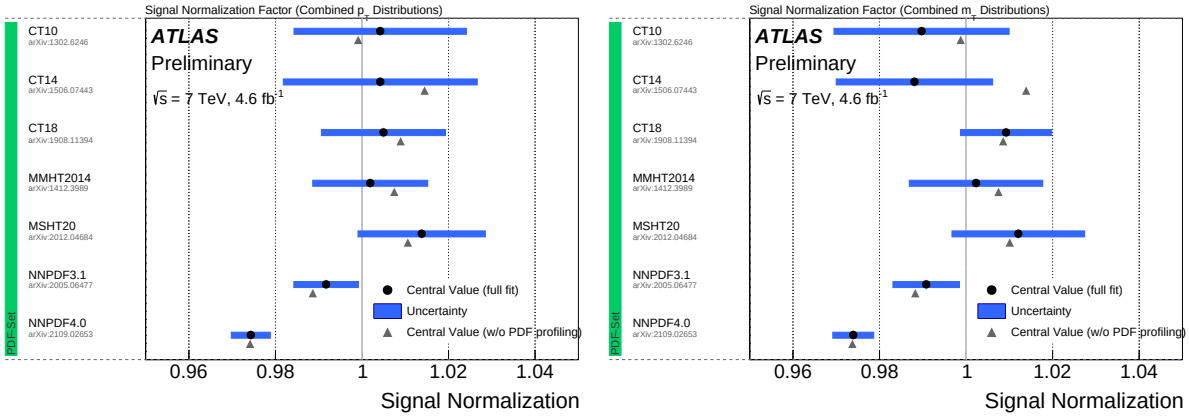

Figure 11: Overview of the global signal normalization factors obtained from the combined PLH fits using the p_{T}^{ℓ} (left) and the m_{T} (right) distributions with different PDF sets. The central values of the normalization factors without PDF profiling in the combined PLH fit are also indicated.

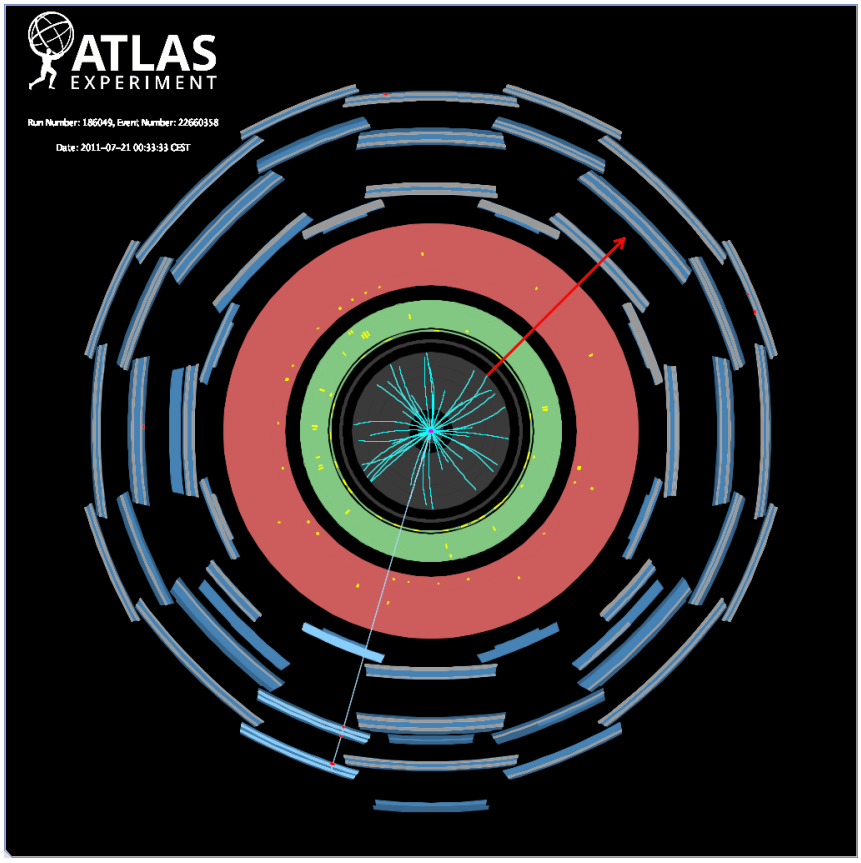

Figure 12: Display of a candidate $W \rightarrow \mu\nu$ event using proton-proton collisions at 7 TeV center of mass energy at the LHC. Starting from the center of the ATLAS detector, the reconstructed tracks of the charged particles in the Inner Detector (ID) are shown as cyan lines. The energy deposits in the electromagnetic (the green layer) and hadronic (the red layer) calorimeters are shown as yellow boxes. The identified muon is shown with its reconstructed track (blue line) passing through the muon chambers (blue layers). The muon has a transverse momentum of $p_{\mathrm{T}} = 36\,\mathrm{GeV}$, whereas the missing transverse energy (red arrow) is 35 GeV and corresponds to the muon neutrino energy. The transverse mass of the W boson candidate is 71 GeV. The view is in the transverse plane.

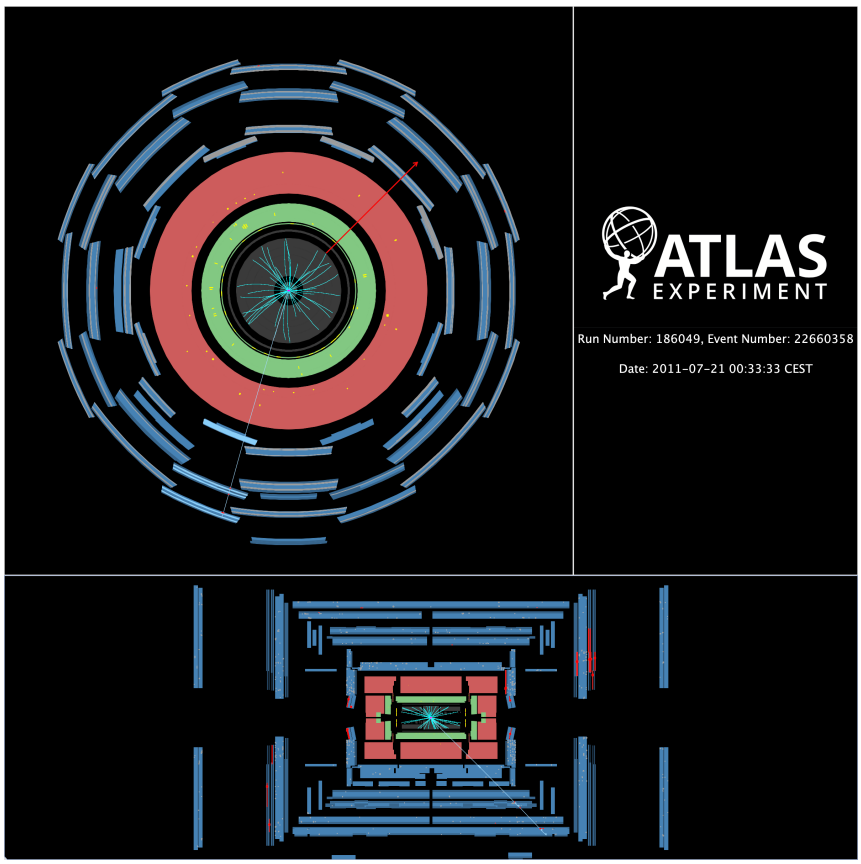

Figure 13: Display of a candidate $W \to \mu\nu$ event using proton-proton collisions at 7 TeV center of mass energy at the LHC. Starting from the center of the ATLAS detector, the reconstructed tracks of the charged particles in the Inner Detector (ID) are shown as cyan lines. The energy deposits in the electromagnetic (the green layer) and hadronic (the red layer) calorimeters are shown as yellow boxes. The identified muon is shown with its reconstructed track (blue line) passing through the muon chambers (blue layers). The muon has a transverse momentum of $p_{\mathrm{T}} = 36\,\mathrm{GeV}$, whereas the missing transverse energy (red arrow) is 35 GeV and corresponds to the muon neutrino energy. The transverse mass of the W boson candidate is 71 GeV. The view at the top shows the transverse plane, while the one at the bottom shows the longitudinal plane. In the longitudinal view, the arrow representing the missing transverse energy has been removed for clarity.

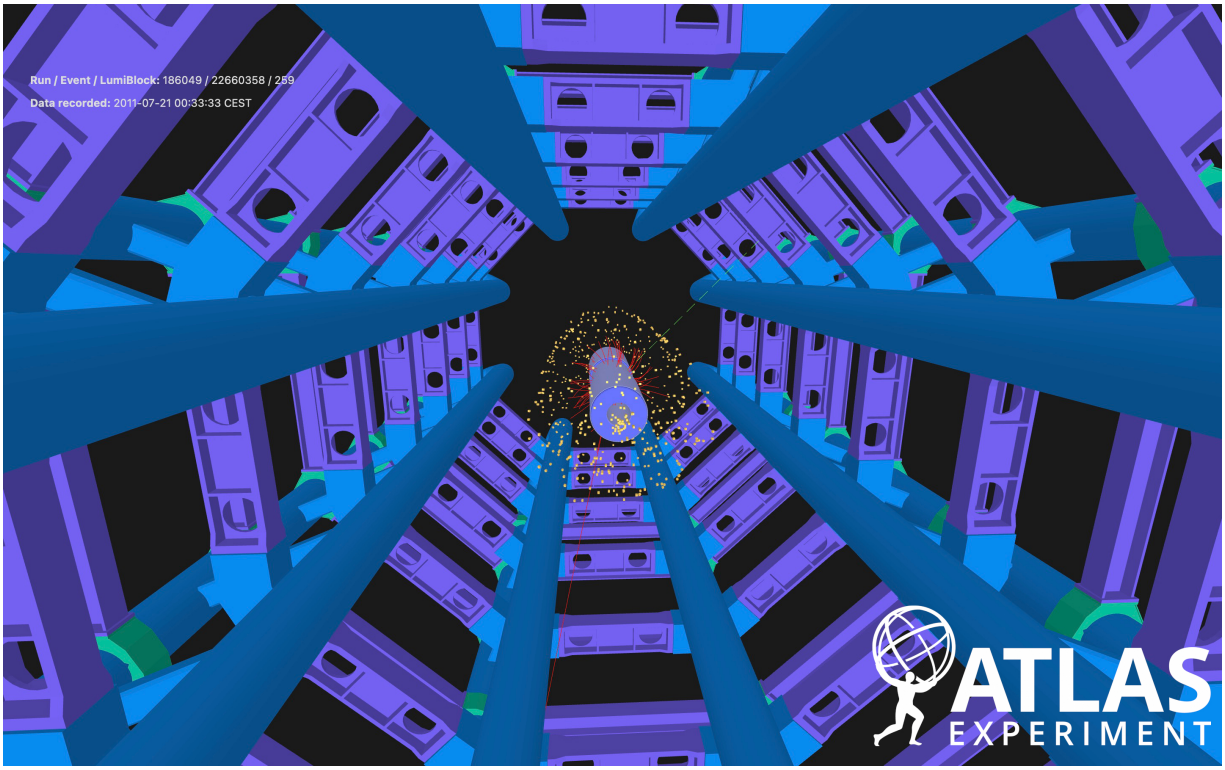

Figure 14: View of a candidate $W \rightarrow \mu\nu$ event using proton-proton collisions at 7 TeV center of mass energy at the LHC. Starting from the center of the ATLAS detector, the reconstructed tracks of the charged particles in the Inner Detector (ID) are shown as red lines. The energy deposits in the calorimeters are shown as yellow boxes. The identified muon is shown as a longer red dashed line. The missing transverse momentum is shown by a green dashed line.